Sinter-HIP WC-17wt% Ni Preforms Fabricated by Binder Jetting Sintered-Agglomerated Powder

Edgar Mendoza Jimenez[1], Olivia Ehrman[1], B. Reeja-Jayan[1], Jack Beuth[1]

[1]*Department of Mechanical Engineering, Carnegie Mellon University, Pittsburgh PA 15213*

ABSTRACT

Binder jet additive manufacturing followed by sintering and hot isostatic pressing (HIP) steps presents an opportunity to fabricate ceramic particle-metal matrix composites parts with greater geometric complexity. In this study, a sintered-agglomerated WC-Ni composite powder with 17 wt.% nickel was used to binder jet green preforms. The effects of sinter-HIP parameters (sintering temperature, sintering duration, and HIP temperature) on porosity, microstructure, hardness and oxidation behavior were evaluated. The highest average relative density produced in this study was 96.8% and shrinkage of these samples was about 64%. Microstructural characterization shows the WC grains are homogenously distributed throughout the nickel matrix and grew to an average diameter of 1.6 μm (a 60% increase) during processing. XRD spectra indicate no unwanted products were formed. Processed samples achieved a maximum hardness of 54.0 Rockwell C, limited by their internal porosity. Oxidation tests show oxidation reactions are dominated by the high WC content and mainly produce WO_3 and $NiWO_4$ at temperatures above 600 ºC. Results from this study further motivate the use of binder jetting to fabricate fully dense, geometrically complex WC-Ni parts with small carbide grains, low nickel content, desirable microstructure, and suitable functional properties.

1. INTRODUCTION

Novel applications are motivating the adoption of ceramic particle-metal matrix composites because they offer superior performance (e.g. high temperature resistance, corrosion resistance, and wear resistance) compared to metal alloys [1]. Ceramic particle-metal matrix composites, commonly known as cermets or cemented carbides, are material systems comprised of ceramic carbide particles (e.g. tungsten carbide, silicon carbide, and titanium carbide) dispersed within a metal binder (e.g. cobalt, nickel, steel). They can exhibit a wide range of mechanical, thermal, and electrical properties that can be adjusted by changing carbide particles, binder content, the ratio between the two phases, and the carbide particle size distribution [2]. WC particles and cobalt (Co) binder is the most frequent cermet combination because of its superior mechanical properties. However, nickel (Ni) is a common binder alternative as it is less magnetic, exhibits greater oxidation resistance, and possesses similar mechanical properties to cobalt [3][4].

Given their high hardness, milling and other forms of subtractive manufacturing are not suitable for fabricating cermet parts. Therefore, cermets are conventionally manufactured using liquid phase sintering and hot isostatic hipping (HIP) techniques. This consist of compacting carbide and metal powders with a die and subjecting the compact to high temperatures (>1300ºC) and pressures (>1 MPa) that causes the binder to melt, wet the carbide particles, and densify the part [5]. Unfortunately, the geometries of these parts are significantly constrained due to the geometric limitations of the powder pressing tools. Cermet coatings can be conventionally manufactured by laser cladding methods, where a laser heats the carbide and metal powders onto a metal substrate which then causes the metal to melt and bind the carbide particles onto the substrate. The volatility of this process, however, can cause the agglomeration and segregation of phases which introduces inhomogeneity within the deposited layers [6]. Although they are not

fully developed, alternative processes that demonstrate the potential of fabricating cermets include vacuum sintering [7], high-frequency induction-heated sintering [8,9], microwave sintering [10], and spark plasma sintering [11–13].

Additive manufacturing (AM) processes present an opportunity to fabricate parts with greater geometric complexity and without the need of additional tooling [14][15][16]. However, the AM of cermets is still at the development stage compared to the established and growing fields of polymer and metal AM [17]. With that said, a variety of additive manufacturing processes have demonstrated the ability to fabricate cermets. The directed energy deposition process can fabricate large grain WC cermets onto a steel substrate [18,19]. Kenyoshi et al. printed WC-Co specimens using the electron beam process [20]. Several publications utilized the laser powder bed fusion (LPBF) process to print with WC-Co [21][22][23][24], WC-Fe[25][26][27], and WC-Ni [28][29][30]. Although some of the LPBF studies printed high density parts, the drastically high temperatures caused by the concentrated laser beam results in the decarburization or decomposition of the carbide and the formation of unwanted complex carbide phases that compromise the functional properties of the final part.

Binder jetting additive manufacturing (BJAM) is an AM process that consolidates powder by using a liquid binder instead of melting it with an energy beam, which can help avoid the formation of unwanted phases during cermet fabrication. The green parts that result from this process possess high amounts of porosity due to the low packing efficiencies of the particles in the powder bed, so they must be further densified with heat treatments like sintering [31,32], infiltrating [33], and/or hot isostatic pressing (HIP) [34,35]. In a series of studies, Cramer et al. manufactured WC-Co cermets by binder jetting WC powder and infiltrating the green parts with Co; they analyzed the effects of various infiltration parameters on functional properties and

managed to fabricate samples with minimal shrinkage [37–39]. However, this approach requires large (>10 μm) WC-particles, which decreases the quality of the final cermet, and final parts exhibit poor shape retention [1]. Enneti et al. demonstrated the ability to binder jet and sinter WC-Co composite powder in a series of studies where they evaluated the effect of processing parameters on printing outputs, sintered green samples to obtain high densities, and characterized mechanical properties of postprocessed sapmle [40–42]; However, non-equilibrium phases in their powder produced coarse clusters of WC within their postprocessed parts, compromising their mechanical properties. In another WC-Co binder jetting study, Mostafaei et al. evaluated the effect of binder saturation and drying time on the microstructure and resulting properties of their printed samples; they showed poor parameter selection could result in defective layer formation and mechanical properties are limited using a mixed, agglomerated powder which creates large pools of matrix material within the sample [43]. In a more recent study, Mariani et al. sinter-HIPed binder jetted WC-12 wt% Co and achieved high densities with mechanical properties similar to conventional processing methods [44].

Previous work in binder jetting cemented carbides establishes their feasibility. However, knowledge regarding the binder jetting of cemented carbides with a nickel matrix and the effect of post processing parameters on final properties is lacking. As such, this study aims to binder jet a WC-Ni sintered-agglomerated composite powder, and post process these preforms using an initial sintering step followed by a HIP step. The effects of sintering temperatures, sintering durations, and HIP temperature on notable properties (e.g. porosity, microstructure, hardness and oxidation behavior) are quantified. Findings from this study provide the details necessary to fabricate dense and geometrically complex WC-Ni cermets for widespread industrial applications.

2. MATERIALS AND METHODS

2.1 Materials

The liquid binder used in the binder jet printing is an aqueous solution provided by ExOne (BA005) and possesses a density of 1.06 g/cm^3. The powder used in this study is a sintered and agglomerated WC-Ni powder (WOKA 3502) manufactured and supplied by Oerlikon Metco (Switzerland). The bulk density of this composite material is 13.85 g/cm^3 given the nominal WC:Ni weight ratio of 83:17. As seen in **Figure 1**, images from a Scanning Electron Microscope (Quanta 600 SEM) shows the powder is spherical in shape and composed of fine (~1 μm) WC particles distributed within a nickel matrix. Hundreds of imaged particles underwent a particle size analysis via ImageJ to quantify the particle size distribution; this analysis shows the composite powder has an average particle diameter of about $24\ \mu m$, D10 value of $10\ \mu m$, D90 value of $45\ \mu m$. The powder was not preprocessed before printing.

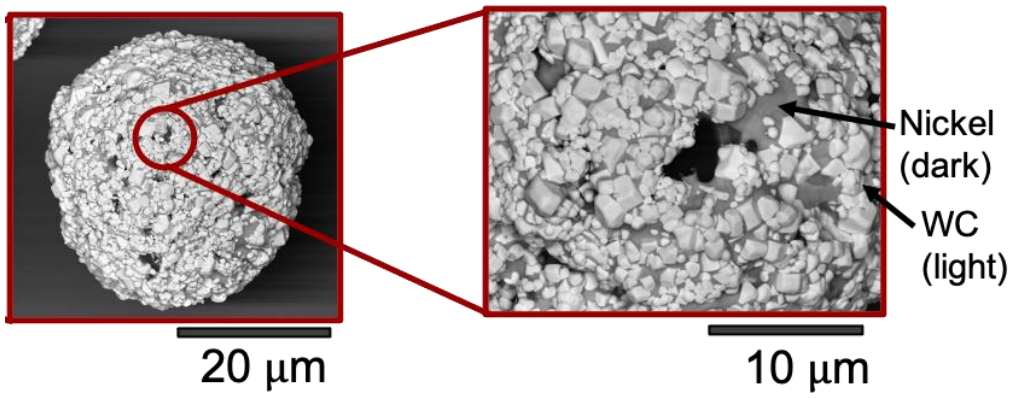

Figure 1: Scanning electron microscopy images of WC-Ni composite powder. WC and nickel phase are shown light and dark grey, respectively. Powder is spherical in shape and posseses fine (~1μm) WC particles uniformly distributed throughout the powder agglomerate.

2.2 Processing

WC-Ni coupons of dimensions 20 mm x 15 mm x 10 mm (length x width x thickness) were binder jetted using the Innovent Machine manufactured by ExOne (North Huntingdon, PA, USA). During the build process, the machine's print head selectively deposits an aqueous binder onto a flat powder bed in the shape of the part cross section. Next, the platform supporting the powder bed lowers to allow for a new layer of powder, and a heat lamp radiates over the powder bed to partially cure the liquid binder. A hopper, which holds fresh powder, then hovers over the powder bed and oscillates to deposit powder that is immediately flattened by a roller. The printhead deposits binder in the shape of the next cross section, and the process repeats until the part is complete. The powder bed is then extracted from the machine and placed into an oven to fully cure the binder at 200 ℃ for 4 hours, per ExOne specifications. After curing, the green parts are durable enough to be gently extracted from the powder bed. Processing parameters used to fabricate the preforms were determined in a preliminary experiment to ensure the deposition of flat, uniform layers and satisfactory green part strength and are shown in **Table 1**. The layer thickness parameter controls the distance the platform is lowered at the start of a new layer, recoat speed is the lateral speed of the powder hopper as it vibrates to deposit fresh powder, oscillator speed is the rate at which the powder hopper vibrates while depositing fresh powder, roller speed is the velocity of the roller as it flattens out the newly deposited powder, drying time controls the duration the heat lamp partially cures the binder at every layer, drying power is the intensity of the heat lamp as it partially cures the binder, and saturation level is the ratio of binder volume to the volume of the interstitial voids within the powder bed.

Intermediate sintering treatments were performed in an argon environment at four different temperatures (1050ºC, 1150 ºC, 1250 ºC, and 1350 ºC) and held for two different durations (1

hour, 6 hours). During ramp up, each sample was held at 500 ºC for 2 hours to ensure the binder fully evaporated and left the specimens before the onset of sintering. A visual depiction of the heating profile can be seen in **Figure 2**, which consist of heating samples to 500 ºC at a rate of 5 ºC/min, hold for 2 hours, heat from 500 ºC to the sintering temperature (T_1) at a rate of 5ºC/min, hold at that temperature for a duration of *t*, and cool down to room temperature at a cooling rate of 5ºC/min. An additional hot isostatic pressing (HIP) step was done on the sintered samples where they were subjected to a pressure of 5 MPa via argon gas at a maximum temperature for 30 min. Three different maximum HIP temperatures were investigated: 1400 ºC, 1425ºC, 1450 ºC. The intermediate sintering temperatures, intermediate sintering durations, and HIP temperatures were tested in full factorial design of experiments, for a total of 24 unique sintering parameter combinations. Four samples were subjected to each heat treatment combination.

Processing Parameters	**Values**
Layer Thickness (μm)	100
Saturation Level (%)	90
Recoat Speed (mm/s)	60
Oscillation Speed (rpm)	3000
Roller Traverse Speed (mm/s)	100
Roller Rotational Speed (rpm)	200
Drying Time (s)	30
Emitter Output (%)	75

Table 1: Processing parameters used to binder jet WC-Ni composite powder in the ExOne Innovent machine.

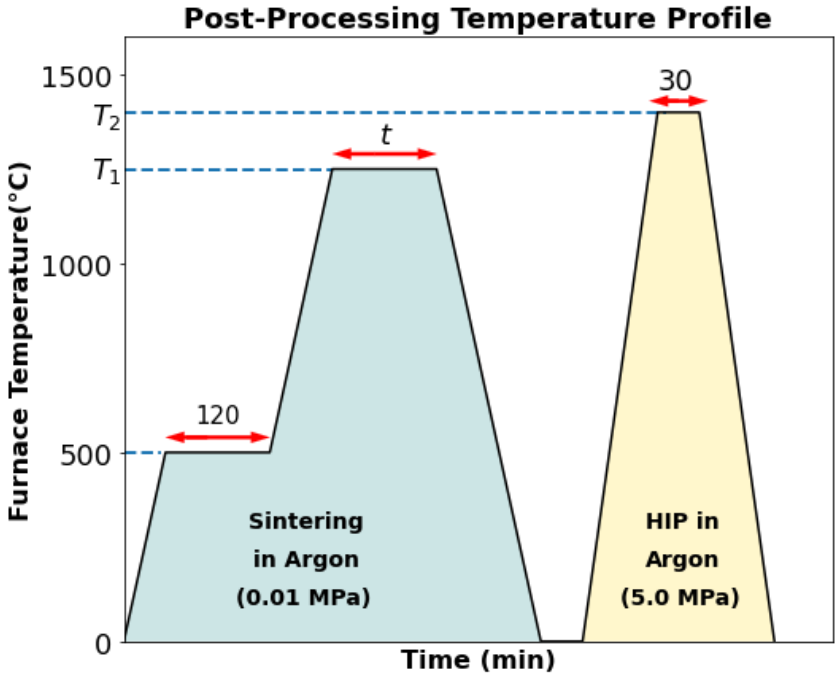

Figure 2: Heating profile for the post-processing step. Samples were heated from room temperature to 500 ºC, held for 120 minutes, heated from 500 ºC to temperature T_1 (1050ºC, 1150 ºC, 1250 ºC, or 1350 ºC), held at that temperature for t (1 or 8 hours), cooled back down to room temperature, and heated to a temperature of T_2 (1400 ºC, 1425 ºC, or 1450 ºC) for 30 minutes. Heating rates were 5ºC/m in. Heating to T_1 was done in argon at ambient pressures, and heating to T_2 was done in argon at a pressure of 5.0 MPa.

2.3 Characterization

Two methods were used to measure the densities of samples after being intermediately sintered and HIP'ed: the geometric approach [45] and Archimedes approach (ASTM C20) [46]. In the geometric approach, the mass of the prism, measured using a Fisher Scientific SLF103 scale with an accuracy of 0.001 g, is divided by its volume, measured with a Vinca DCLA-0605 digital caliper that has a resolution of 0.01 mm. In the Archimedes approach, the density is calculated using the following equation:

$$\rho = \frac{W_{air}}{W_{air} - W_{water}} \times \rho_{liquid}$$

Where W_{air} is the weight of the prism measured in air, W_{water} is the weight of the prism submerged in water, and ρ_{liquid} is the density of water (~1.00 g/cm^3). Weight measurements for the Archimedes method were also taken with the Fisher Scientific SLF103 scale. Relative densities were calculated by dividing the measured density with the theoretical bulk density. The theoretical bulk density of the WC-17 wt.% Ni composite is 13.95 g/cm^3, as determined by the rule of mixtures in which the theoretical densities of WC and Ni are 15.63 g/cm^3 and 8.90 g/cm^3, respectively.

Density measurements underwent a main effect to measure the influence of each processing parameter. A main effect analysis is utilized to qualitatively compare the influence of each process parameter on the experimental response (i.e. final densities). A main effect analysis is utilized to qualitatively compare the influence of each process parameter on the experimental response (i.e. sintered densities). The effect of a parameter *A* at the level *i* ($E_{A(i)}$) on the response *Y* is computed using the following equation:

$$E_{A(i)} = \bar{Y}_{A(i)}$$

where $\bar{Y}_{A(i)}$ is the average of all the responses when the parameter A is at the level i, regardless the value of other parameters. An input's main effect (F_A) is defined as the range of the parameter's effects at different levels:

$$F_A = \mathrm{Max}\left(E_{A(i)}\right) - Min\left(E_{A(i)}\right)$$

The main effect analysis assumes the process parameter are not interdependent, which is the case for the sintering parameters in this study. The larger the magnitude of the main effect, the more influence the process input has on the measured output.

One sample from each parameter combination was prepared for SEM imaging. These samples were sectioned with a diamond blade, cold mounted in resin, and polished down to 1µm using diamond suspension, per ASTM B665 [47]. SEM images underwent particle analyses to quantify the apparent porosity using ImageJ software, per ASTM B276; relative densities were calculated as the inverse of the resulting apparent porosity.

X-Ray Diffraction (XRD) analyses were carried out on raw powder, intermediately sintered samples, and HIP'ed samples investigate changes in the chemical composition (PANalytical X'Pert Pro, United Kingdom) at each processing step. XRD diffraction patterns were collected with 2θ steps of 0.02º and 120 µs of acquisition time. Scanning Electron Microscopy (SEM) and Energy Dispersive X-Ray (EDX) Analysis were performed in a Quanta 600 Microscope using a secondary electron detector at an operating voltage of 15kV and a working distance of 10 mm.

To evaluate mechanical properties of the processed cemented carbides, hardness on the macro-scale is evaluated. The macrohardness of each HIP'ed sample was measured on the Rockwell C (HRC) scale using a Wilson Rockwell 2000 Hardness Tester per ASTM E18 [48]. For

these tests, a coupon with a minimum thickness of 5 mm was sectioned along the build direction. Ten measurements were taken at different locations for each sintered sample.

Oxidation behavior of the processed cemented carbides with 4-6% porosity was studied under isothermal heating at 500ºC, 600 ºC, 700 ºC, and 800ºC in air (4 samples per temperature). Samples were sectioned into 10 x 7 mm couples with thicknesses varying between 2-3 mm. Then they were inserted into a furnace and held at the specified furnace temperature. Samples were weighed every hour for up to 5 hours. The mass gain per unit surface area was calculated to estimate the oxidation. The identification of crystalline phases in the oxidized sample was carried out by XRD.

3. RESULTS AND DISCUSSION

3.1 Green and Intermediately Sintered Samples

The processing parameters listed in **Table 1** produced samples that exhibited satisfactory powder flowability, geometric shape retention, and green part strength. A printed sample can be seen in **Figure 3**. The average packing efficiency and relative density of the printed samples was about 35% with a standard deviation of $\pm$2%, as measured by the volumetric density approach.

Average density measurements (volumetric and Archimedes) after the intermediate sintering step are shown in **Table 2**. Densities are the highest and lowest when samples are intermediately sintered at the highest temperature (1350ºC) and lowest temperature (1050 ºC), respectively; this is expected since sintering and densification activity are heavily influenced by processing temperatures. Archimedes and volumetric densities of samples processed at the highest and lowest temperatures are similar, with an average difference of 2.3% between the two approaches. Both density approaches show average densities are higher in samples held for 8 hours at the sintering temperature compared to samples held for 1 hour at the same temperature; this is expected since longer heating durations allows more time for atomic movement and densification. However, the increase in Archimedes densities is not drastic (<10%) and the difference is smaller for the volumetric densities (<3%).

There are large discrepancies between the two density approaches for samples intermediately sintered at the two medial temperatures, 1150 ºC and 1250 ºC. These discrepancies are visualized in **Figure 4**, where density measurements are averaged at each intermediately sintered temperature. According to volumetric densities, no noticeable densification occurs below 1350 ºC but, according to Archimedes measurements, sample densities increase with every temperature increase. The difference in measurements between the two approaches can be

attributed to the inherent nature of each approach [49]. In the Archimedes approach, the fluid must completely fill the porosity to take it into account. Therefore, this approach only considers open porosity, and any closed porosity is treated as part of the solid material. In the volumetric approach, both open and closed porosities are considered since they are massless when the sample is weighed. As such, the volumetric density can be considered the "true" density of the samples, and the increase in the Archimedes density is a result of the open porosity transitioning to closed porosity (i.e. the permeability of the samples decrease with increasing sintering temperatures). A sintered sample that did not experience significant densification is shown in **Figure 3.** Note, the sample maintains its porous appearance and texture.

There is noticeable shrinkage only for the samples intermediately sintered at 1350 ºC, characterized by the increase in volumetric density shown in **Figure 4**. This shrinkage can be attributed to the change in phases of the nickel matrix. This material system (WC:Ni 83:17 wt.%) possesses a eutectic point at approximately 1300 ºC [50]; therefore, a solid WC phase coexists with a liquid nickel phase at temperatures above 1300 ºC. For samples sintered under 1300 ºC, the change in porosity is attributed to the solid-state sintering of the nickel phase. However, the liquid nickel phase present in samples sintered above 1300 ºC causes an increase in densification as it allows for the rearrangement of the solid carbide particles by capillary forces.

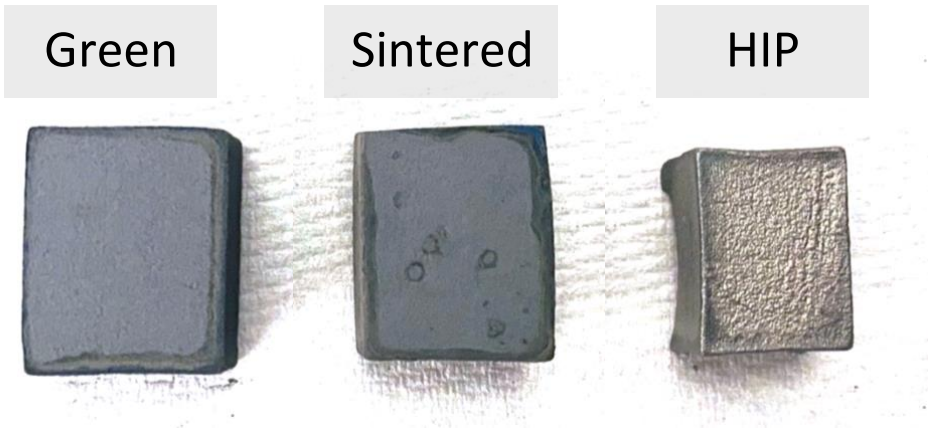

Figure 3: Samples after each processing step. [Left] Green preform immediately after binder jetting and before post processing. [Center] Sample after it was exposed to the intermediate sintering step. [Right] Sample after it was exposed to the HIP step.

Table 2: Average volumetric and Archimedes relative density measurements for sintered samples at every parameter combination.

Intermediate Sintering Parameters		**Density Measurements**	
Sintering Temperature, T_1 (ºC)	**Sintering Duration, *t* (Hours)**	**Volumetric Relative Density**	**Archimedes Relative Density**
1350	8	**76.6** ± 2.0%	**77.1** ± 2.1%
1350	1	**72.9** ± 2.5%	**72.5** ± 2.6%
1250	8	**38.0** ± 1.3%	**61.4** ± 1.0%
1250	1	**36.9** ± 2.2%	**55.2** ± 1.5%
1150	8	**37.0** ± 1.2%	**53.0** ± 2.5%
1150	1	**36.8** ± 1.0%	**52.3** ± 1.4%
1050	8	**36.4** ± 1.5%	**41.7** ± 3.1%
1050	1	**34.2** ± 1.6%	**36.1** ± 2.5%

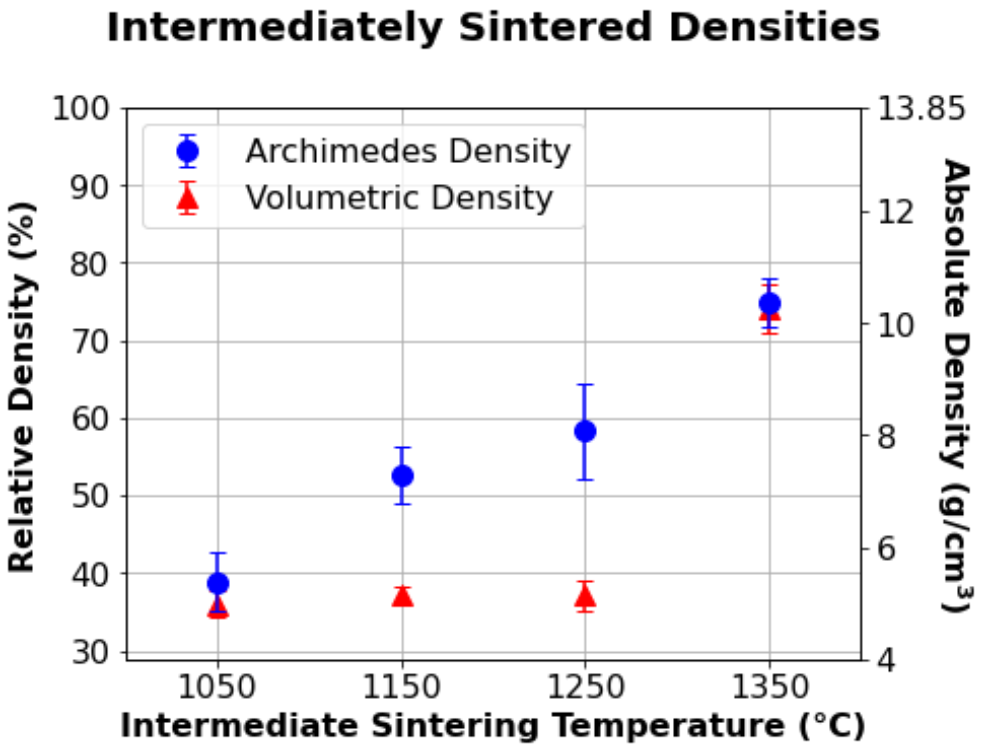

Figure 4: Densities of the intermediately sintered WC-Ni samples. Archimedes and volumetric densities of the samples averaged as a function of sintering temperature. Absolute densities are labeled on the left y-axis and the corresponding relative densities are labeled on the right y-axis.

3.2 Final Densities

Average density measurements (volumetric and Archimedes) for every post processing parameter combination are tabulated in **Table 3.** Given the fact that all samples exceeded a relative density of 85%, it is necessary to incorporate a HIP step in the post processing of binder jetted cemented carbides. A HIP sample is shown in **Figure 3**; the sample's high density gives it a smaller appearance, smoother texture, and glossy finish. The response of every parameter (sintering temperature, sintering duration, and HIP temperature) is shown in **Figure 5**. There is a systematic increase in density with every increasing parameter. As previously mentioned, a parameter's main effect is found by calculating the range between averages for that specific parameter; a larger range implies a larger influence. Ordering parameters by the magnitude of their main effect gives the following ranking: ***Sintering Temperature (T_1) > HIP Temperature (T_2) > Sintering Duration HIP Temperature (t)***. Given the specific parameters selected in this study, the most influential parameter was sintering temperature. The average relative density of samples sintered at 1350 ºC was about 93%, while the average relative density of samples omitted from the intermediate sintering step (labeled as "N/A") was about 88%. HIP temperature was the second most influential parameter with a relative density difference of 3.40% between the samples HIP'ed at 1400 ºC and the samples HIP'ed at 1450 ºC. Intermediate sintering duration was the least influential parameter with a difference of 3.16% between samples sintered for 8 hours and the samples omitted from intermediate sintering. When only comparing samples that were intermediately sintered, the difference in average relative density between samples sintered for 1 and 8 hours further decreases to 0.5%. This suggests the effect of intermediate sintering duration is minimal and a short duration would suffice in realizing significant densification during sinter-HIP of binder jetted WC-Ni parts.

The highest volumetric densities were reached at a HIP temperature of 1450 ºC, an intermediate sintering temperature of 1350 ºC, and intermediate sintering durations of 1 and 8 hours with average densities of 96.8% and 95.1%, respectively. The volumetric shrinkage witnessed in theses samples was about 64%. For all samples, it can be stated that HIP had a significant effect on the reduction of porosity and is necessary to achieve high densities for binder jetted WC-Ni parts. The mechanisms involved in densifying cemented carbides during HIP are diffusion bonding and liquid phase sintering of the metal matrix [1]. However, these mechanism could not achieve fully dense samples.

Figure 6 consists of optical images showing the cross section of samples HIP'ed at 1450 ºC for different intermediate sintering parameter combinations. The pores are circular and closed in nature, with their quantity and size decreasing as sintering temperature is increased. These pores are caused by the formation of gas/vapor pockets during the intermediate sintering and HIP steps. The presence of the trapped gas in the pores act as a densification resistance factor so as the samples densify, shrinking of these pockets is limited. Cermet studies that conventionally fabricated preforms and achieved full densities after sinter-HIP only did so when the sintering processes was done in a vacuum, without a gaseous medium [51]. Therefore, one must intermediately sinter binder jetted WC-Ni samples in a vacuum to further reduce porosity and achieve full densities.

Table 3: Density values tabulated for sinter-HIP'ed samples

Post Processing Parameters			**Density Measurements**	
Sintering Temperature, T_1 (ºC)	**Sintering Duration, t (Hours)**	**HIP Temperature, T_2 (ºC)**	**Average Volumetric Relative Density**	**Average Archimedes Relative Density**
1350	8	1450	**95.1** ± 3.4%	**97.6** ± 1.2%
1350	8	1425	**91.5** ± 2.5%	**95.5** ± 1.8%
1350	8	1400	**90.2** ± 3.1%	**92.9** ± 2.0%
1350	1	1450	**96.8** ± 1.3%	**97.3** ± 2.6%
1350	1	1425	**93.4** ± 2.4%	**95.1** ± 1.6%
1350	1	1400	**91.1** ± 3.2%	**91.8** ± 2.2%
1250	8	1450	**93.8** ± 2.5%	**93.8** ± 0.4%
1250	8	1425	**91.5** ± 2.9%	**91.5** ± 2.5%
1250	8	1400	**88.6** ± 3.1%	**88.6** ± 2.2%
1250	1	1450	**91.2** ± 2.8%	**91.2** ± 1.0%
1250	1	1425	**90.9** ± 2.6%	**90.9** ± 2.5%
1250	1	1400	**88.3** ± 2.6%	**88.3** ± 1.3%
1150	8	1450	**92.8** ± 2.8%	**92.8** ± 0.6%
1150	8	1425	**89.5** ± 3.2%	**89.5** ± 0.9%
1150	8	1400	**89.3** ± 1.8%	**89.3** ± 1.6%
1150	1	1450	**90.1** ± 2.6%	**90.1** ± 1.8%
1150	1	1425	**88.7** ± 3.6%	**88.7** ± 2.1%
1150	1	1400	**88.6** ± 2.9%	**88.6** ± 2.5%
1050	8	1450	**91.1** ± 3.5%	**91.1** ± 0.8%
1050	8	1425	**89.4** ± 2.9%	**89.4** ± 2.1%
1050	8	1400	**88.9** ± 3.1%	**88.9** ± 2.3%
1050	1	1450	**89.5** ± 3.2%	**89.5** ± 2.1%
1050	1	1425	**88.7** ± 1.1%	**88.7** ± 2.6%
1050	1	1400	**87.8** ± 3.0%	**87.8** ± 1.9%
N/A	N/A	1450	**90.1** ± 4.0%	**97.8** ± 1.2%
N/A	N/A	1425	**86.5** ± 4.1%	**96.8** ± 0.4%
N/A	N/A	1400	**90.1** ± 4.3%	**93.6** ± 2.0%

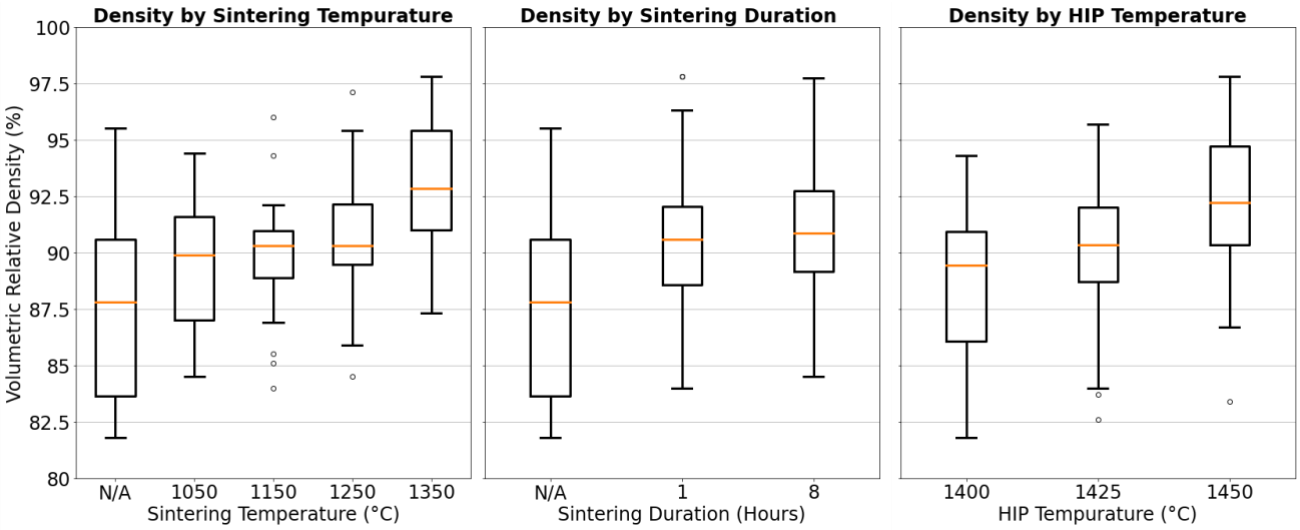

Figure 5: Effect of each post processing parameter on volumetric relative density

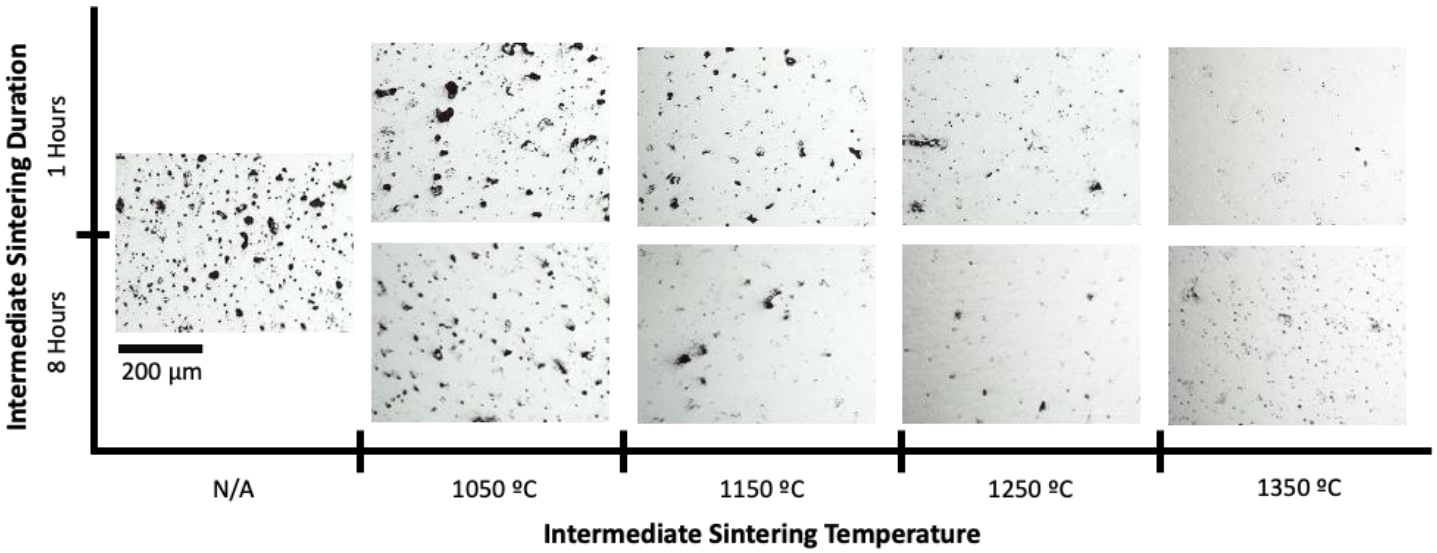

Figure 6:Optical images showing the cross section of samples HIP'ed at 1450 ºC. Different cross sections are shown for different intermediate sintering parameter combinations.

3.3 Microstructure

Microstructure was consistent throughout all the HIP'ed samples. **Figure 7** shows an SEM image of the cross section of the densest sample after sinter-HIP. The microstructure consists of WC particles (bright grey) in a Ni matrix (dark areas). The carbide particles are homogenously distributed throughout the nickel with no large (>10 μm) pooling of the matrix observed. The WC particles kept their angular morphology that was present in the powder. The post processing conditions increased grain contiguity, as shown by grain coalescence between particles that are in contact with each other.

Figure 8 plots the WC grain size distribution within the raw powder and HIP'ed samples, as measured by the line intercept method on SEM images. The size of the WC grains increases after processing; the powder possessed an average grain diameter of about 1.0 ± 0.6 μm, and the sinter-HIP'ed samples possessed an average grain diameter of 1.6 ± 0.9 μm. This grain growth, quantified by a ~60% increase in average grain diameter, can be attributed to two phenomena during the sintering densification process [52]. The first is solid phase sintering in which WC grains combine and grow by surface diffusion when they are in contact with each other. The second is liquid phase diffusion in which small WC particles melt by the presence of the Ni-rich liquid phase, diffuse through the liquid, and then precipitated on the surface of coarse WC particles, resulting in WC particle size growth.

Normalized XRD spectra for a powder sample, an intermediately sintered sample, and a HIP'ed sample are shown in **Figure 9**. Peaks for only WC and Ni exist for all three samples. This suggests all the binder was burnt out of the sample, oxidation did not occur, and no unwanted products were formed during processing. The lack of carbide products is due to the high purity of

the powder, as it has been shown that powder impurities (e.g. W_2C, Ni(W,C), etc.) are nucleation points for the formation of unwanted complex carbides [13].

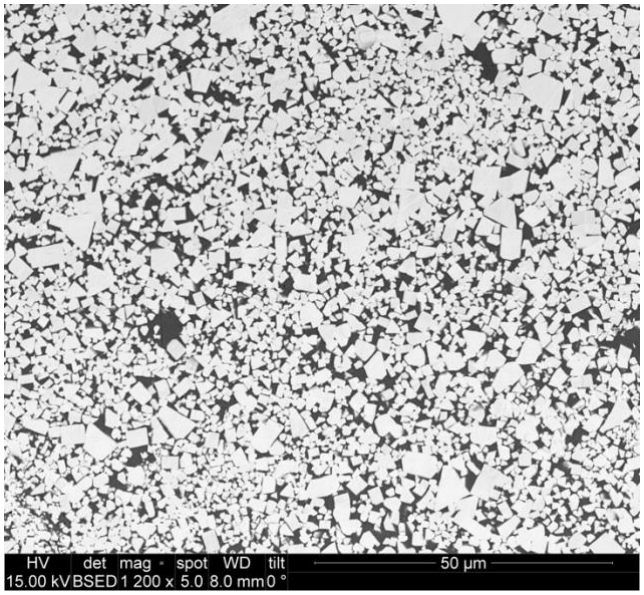

Figure 7: SEM image showing microstructure of a HIP'ed sample processed with an intermediate sintering temperature of 1350 ºC, intermediate sintering duration of 1 hour, and HIP temperature of 1450 ºC.

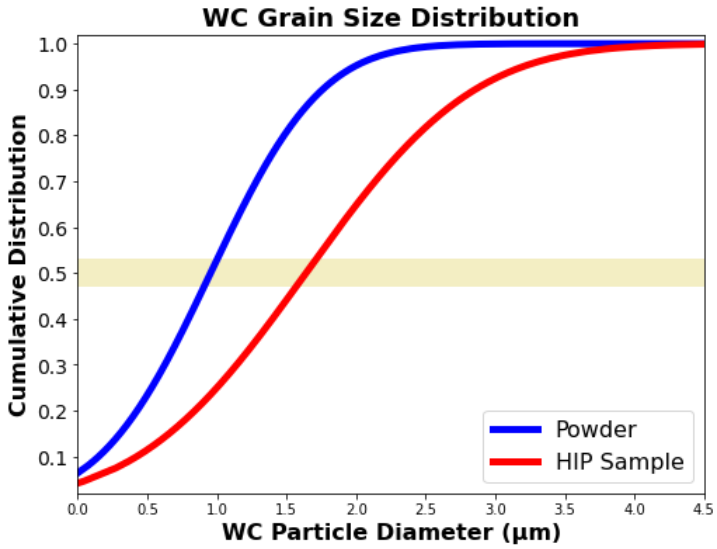

Figure 8: Size distribution of WC grains in powder (blue line) and HIP'ed samples (red line) as measured by the line-intercept method.

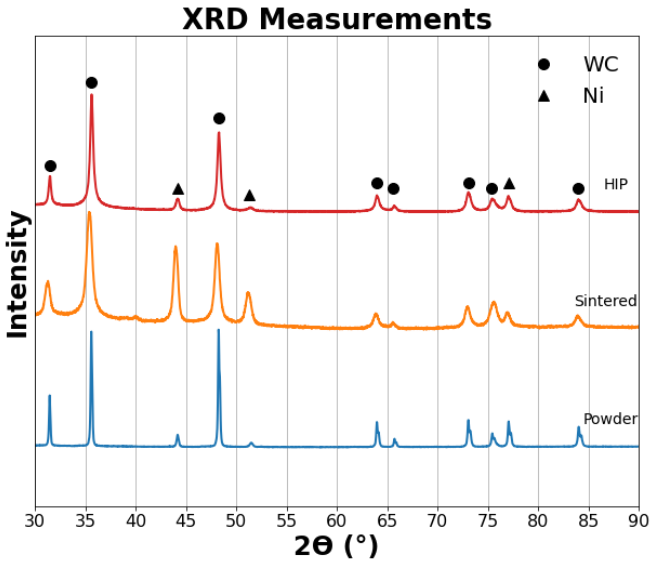

Figure 9: XRD spectra of powder, an intermediately sintered sample, and a HIP'ed sample

3.4 Hardness

Rockwell C hardness values of the WC-Ni samples after sinter-HIP are plotted as a function of their respective porosity in **Figure 10**. The average hardness varied between 54 and 45 Rockwell C, and the maximum hardness was achieved in the sample with the lowest porosity (3.2%). Hardness decreased as porosity increased, and this is primarily due to the pores within the material collapsing under load during testing. Therefore, the higher the frequency and size of pores, the lower the sample's resulting hardness. If the nominal hardness of this fully dense material is 60 Rockwell C (as specified by the powder vendor), then the hardness decreases in a logarithmic behavior. Least squares fit of the measurements predicts the relationship between hardness and porosity to be:

$$Hardness = 54.5 - 2.7 * log(P)$$

where *P* is porosity (in percentage form). This fit is projected in **Figure 10** and shows decent fit with the measured values. The hardness of a cermet systems is nontrivial since it is dependent on the metal matrix, carbide particle size, and volume ratio between metal matrix and carbide particle. In general, hardness typically decreases with increasing nickel content and WC grain size. For a nickel wt % (17 wt%) and carbide size (1.5 μm) similar to this study, previous literature measured hardness to be within the range of 60-62 Rockwell C [30,53]. The relatively lower hardness from this study can be attributed to the higher porosity within the samples.

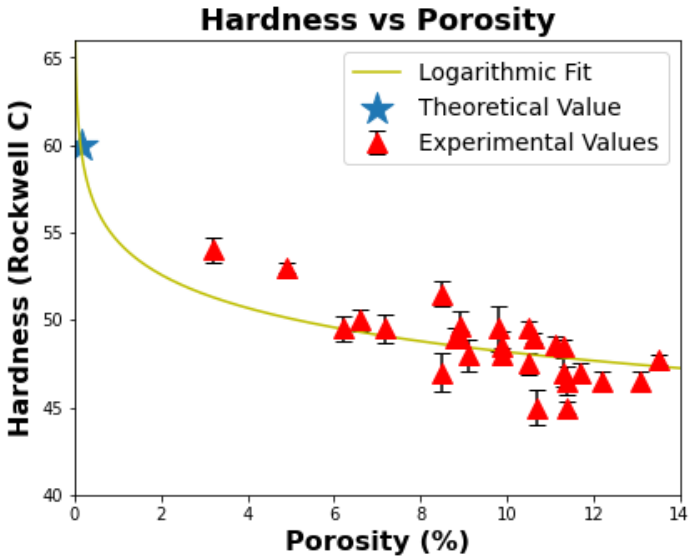

Figure 10: Hardness values of sinter-HIP samples plotted against their respective porosity. Hardness is indirectly correlated with porosity.

3.5 Oxidation

The evolution of mass gain per unit area as a function of time for various temperatures (500, 600, 700, and 800 ºC) is shown in **Figure 11**. As expected, mass gain increased with temperature and time. Mass gain is linear for the lower three isotherms; an average mass gain of 0.4 mg/cm^2, 3.2 mg/cm^2, and 45 mg/cm^2 was achieved after exposing the samples to 500 ºC, 600 ºC, and 700 ºC (respectively) for 5 hours. Oxidation at 800 ºC follows an exponential trend where the rate of mass gain decreases with time and plateaus within 3 hours at about 200 mg/cm^2. **Figure 12** shows images of samples that were oxidized for 5 hours at each isotherm. Samples oxidized at 500 ºC showed no change in color during furnace heating. Samples oxidized at 600 ºC formed a thin green film on the surface. This green film began to grow on samples oxidized at 700 ºC, with swelling observed on the surface of the samples. Drastic swelling occurred on the samples oxidized at 800 ºC. Spalling was also observed after 2 hours of being oxidized at 800 ºC.

XRD spectra for a sample before oxidation and samples oxidized at each isotherm are shown in **Figure 13.** Peaks for the WC and Ni phases are present in the pristine sample and in the sample oxidized at 500 ºC. The WC-Ni material system follows a complex oxidation behavior as it produces both solid and gaseous oxidation products. According to the thermodynamic calculations published in [54], oxidizing WC-Ni at 500 ºC produces $WO_{3(S)}$, $C_{(s)}$, $CO_{(g)}$, $CO_{2(g)}$. A WO_3 peak at about 23º in the 500 ºC spectrum indicates these reactions are present in this study. Unfortunately, WO_3 offers little protection against oxidation and allows oxygen to further diffuse into the material. As a result, new peaks indicating the formation of tungsten oxides (WO_3 and $NiWO_4$) are present for temperatures above 600 ºC. A small presence of NiO is detected at temperatures above 700 ºC. Nickel's oxidative resistant behavior mitigates the formation of NiO and is the reason why the oxide products present in the samples mainly consist of tungsten oxides.

Therefore, the oxidation resistance of these binder jetted parts is dominated by their high WC content and should not be operated at 600ºC and above.

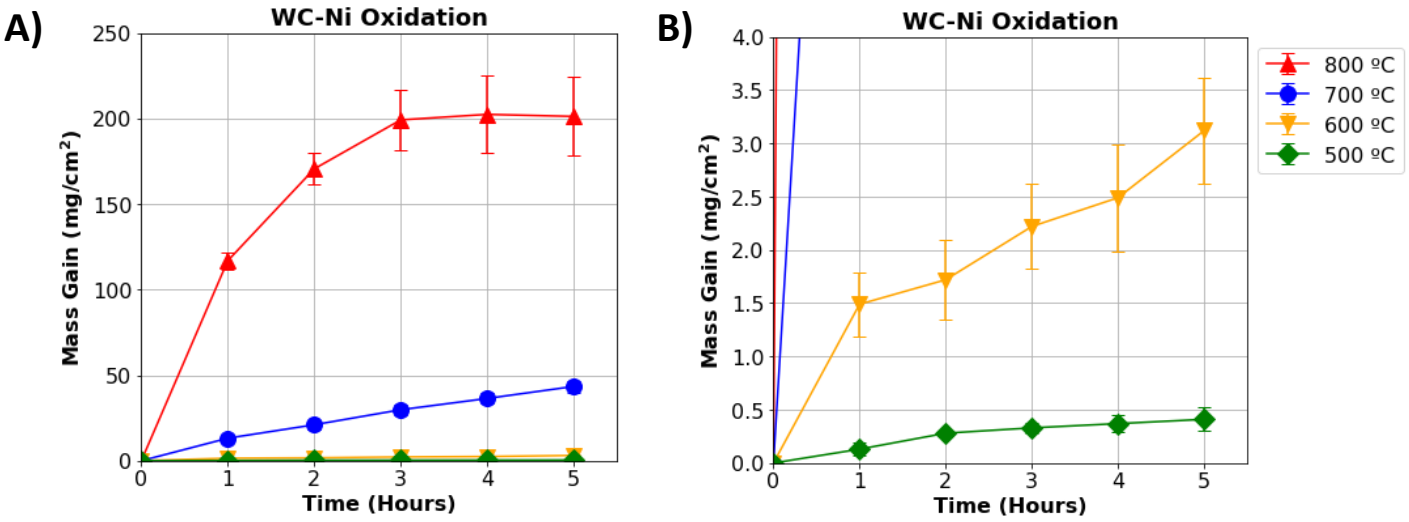

Figure 11: Mass gain as a function of time for various furnace temperatures (500, 600, 700, and 800ºC). Testing was performed in ambient conditions.

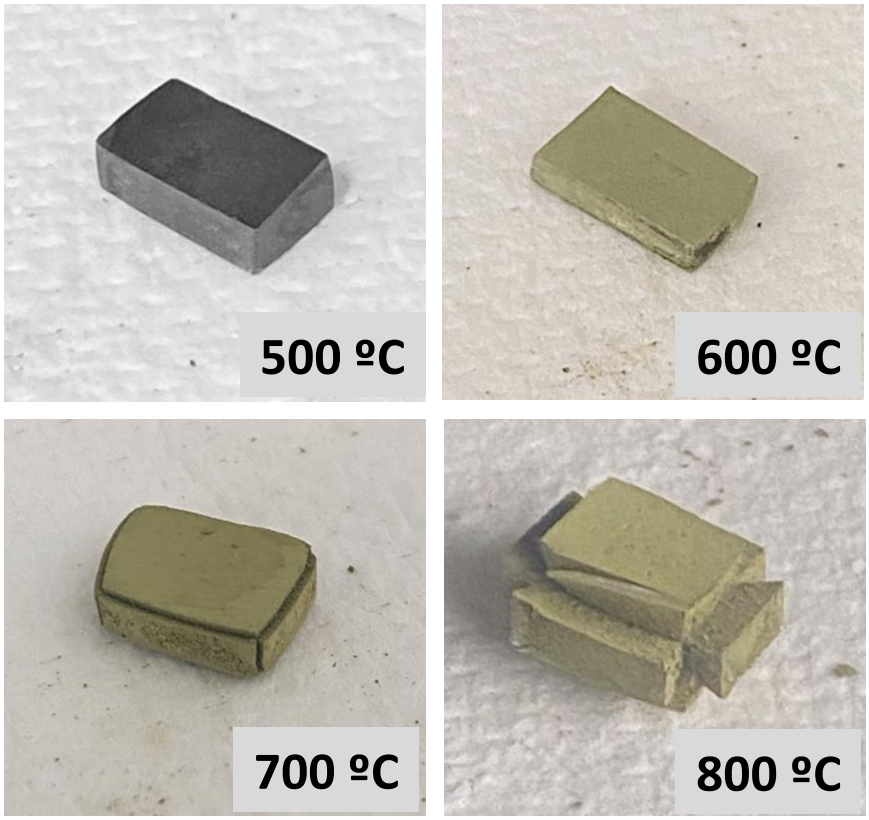

Figure 12: Samples that were oxidized for 5 hours at 500 ºC, 600 ºC, 700 ºC, and 800 ºC.

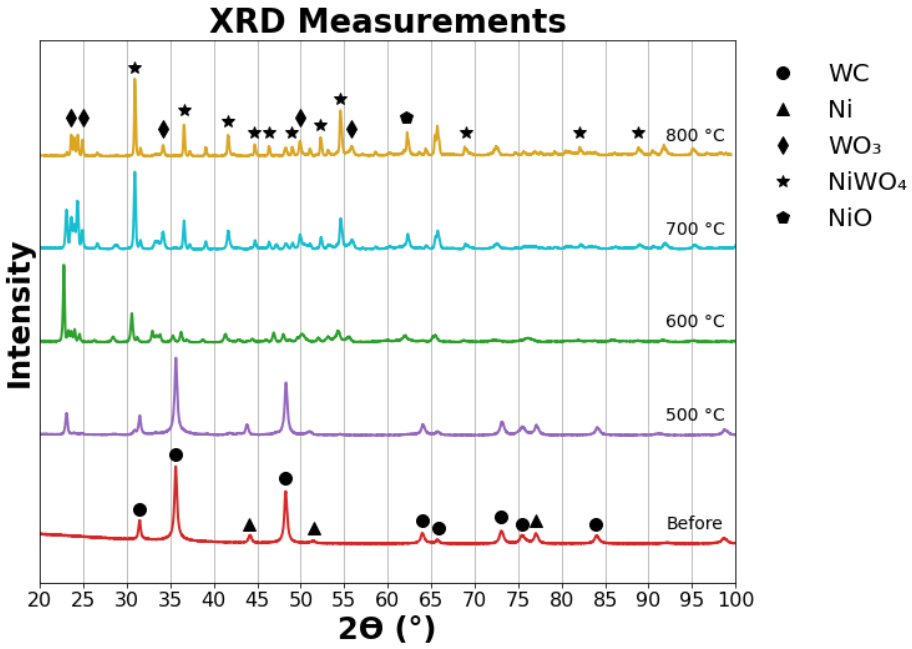

Figure 13: XRD spectra for a sample before oxidation and samples oxidized at different isothermals.

CONCLUSION

In this study, a sintered-agglomerated WC-Ni composite powder with 17 wt.% nickel was used to binder jet green preforms. These preforms were post processed using an initial sintering step followed by a hot isostatic pressing (HIP) step. This heating profile was parametrized to understand the effects of sintering temperatures, sintering durations, and HIP temperature on porosity, microstructure, hardness and oxidation behavior. Final densities of the sinter-HIP samples are positively correlated with every parameter. The highest relative densities are achieved at a HIP temperature of 1450 ºC, a sintering temperature of 1350 ºC, and sintering durations of 1 and 8 hours with average densities of 96.8% and 95.1%, respectively. The volumetric shrinkage witnessed in theses samples is about 64%. Remaining porosity within the samples is caused by the formation of gas or vapor pockets during post processing. To further increase final densities, the authors recommend replace the intermediate sintering step with a vacuum sintering one that remove the gaseous medium. Scanning electron microscopy shows the microstructure was consistent throughout all the parameter combinations. The carbide particles are homogenously distributed throughout the nickel matrix with no large (>10 μm) pooling of the matrix observed. The post processing conditions increased grain contiguity, as particles coalesced when they were in contact with each other. The WC grains had an average diameter of 1.6 μm, experiencing a ~60% growth during processing. XRD spectra indicate no unwanted products were formed. Hardness is indirectly correlated with porosity and the relationship appears to be exponential. The maximum hardness (54.00 Rockwell C) is lower than the values measured in other studies with similar WC grain sizes and nickel content (60-62 Rockwell C), which can be attributed to the higher porosity within the samples fabricated in this study. Oxidation testing of these binder jetted samples show oxidation reactions are dominated by the high WC content. Parts produced with the

methods form this study should avoid operating temperatures above 600 ºC or else a significant amount of WO_3 and $NiWO_4$ will be produced on the part's surface. The successful builds in this study further motivate the use of binder jet additive manufacturing for the fabrication of fully dense, geometrically complex WC-Ni parts with small carbide grains, low nickel content, desirable microstructure, and adequate functional properties.

References

[1] J. García, V. Collado Ciprés, A. Blomqvist, B. Kaplan, Cemented carbide microstructures: a review, Int. J. Refract. Met. Hard Mater. 80 (2019) 40–68. doi:10.1016/j.ijrmhm.2018.12.004.

[2] A.O. Inegbenebor, C.A. Bolu, P.O. Babalola, A.I. Inegbenebor, O.S.I. Fayomi, Aluminum Silicon Carbide Particulate Metal Matrix Composite Development Via Stir Casting Processing, Silicon. 10 (2018) 343–347. doi:10.1007/s12633-016-9451-7.

[3] W. Midlands, Nickel in hardmetals, Met. Powder Rep. 48 (1993) 46. doi:10.1016/0026-0657(93)90317-l.

[4] A.M.F. Rocha, A.C. Bastos, J.P. Cardoso, F. Rodrigues, C.M. Fernandes, E. Soares, J. Sacramento, A.M.R. Senos, M.G.S. Ferreira, Corrosion behaviour of WC hardmetals with nickel-based binders, Corros. Sci. 147 (2019) 384–393. doi:10.1016/j.corsci.2018.11.015.

[5] E.A. Almond, B. Roebuck, Identification of optimum binder phase compositions for improved WC hard metals, Mater. Sci. Eng. 105–106 (1988) 237–248. doi:10.1016/0025-5416(88)90502-2.

[6] K. Van Acker, D. Vanhoyweghen, R. Persoons, J. Vangrunderbeek, Influence of tungsten carbide particle size and distribution on the wear resistance of laser clad WC/Ni coatings, Wear. 258 (2005) 194–202. doi:10.1016/j.wear.2004.09.041.

[7] S.H. Chang, S.L. Chen, Characterization and properties of sintered WC-Co and WC-Ni-Fe hard metal alloys, J. Alloys Compd. 585 (2014) 407–413. doi:10.1016/j.jallcom.2013.09.188.

[8] I.J. Shon, I.K. Jeong, I.Y. Ko, J.M. Doh, K. Do Woo, Sintering behavior and mechanical properties of WC-10Co, WC-10Ni and WC-10Fe hard materials produced by high-

frequency induction heated sintering, Ceram. Int. 35 (2009) 339–344. doi:10.1016/j.ceramint.2007.11.003.

[9] H.C. Kim, I.J. Shon, J.K. Yoon, J.M. Doh, Z.A. Munir, Rapid sintering of ultrafine WC-Ni cermets, Int. J. Refract. Met. Hard Mater. 24 (2006) 427–431. doi:10.1016/j.ijrmhm.2005.07.002.

[10] E. Breval, J.P. Cheng, D.K. Agrawal, P. Gigl, M. Dennis, R. Roy, A.J. Papworth, Comparison between microwave and conventional sintering of WC/Co composites, Mater. Sci. Eng. A. 391 (2005) 285–295. doi:10.1016/j.msea.2004.08.085.

[11] H.C. Kim, D.Y. Oh, I.J. Shon, Sintering of nanophase WC-15vol.%Co hard metals by rapid sintering process, Int. J. Refract. Met. Hard Mater. 22 (2004) 197–203. doi:10.1016/j.ijrmhm.2004.06.006.

[12] H. Rong, Z. Peng, X. Ren, Y. Peng, C. Wang, Z. Fu, L. Qi, H. Miao, Ultrafine WC-Ni cemented carbides fabricated by spark plasma sintering, Mater. Sci. Eng. A. 532 (2012) 543–547. doi:10.1016/j.msea.2011.10.119.

[13] E. Ghasali, T. Ebadzadeh, M. Alizadeh, M. Razavi, Mechanical and microstructural properties of WC-based cermets: A comparative study on the effect of Ni and Mo binder phases, Ceram. Int. 44 (2018) 2283–2291. doi:10.1016/j.ceramint.2017.10.189.

[14] A. Goulas, R.J. Friel, U. Kingdom, Laser Sintering of Ceramic Materials for Aeronautical and Astronautical Applications, (2017).

[15] D.D. Gu, W. Meiners, K. Wissenbach, R. Poprawe, Laser additive manufacturing of metallic components: Materials, processes and mechanisms, Int. Mater. Rev. 57 (2012) 133–164. doi:10.1179/1743280411Y.0000000014.

[16] E. Mendoza Jimenez, D. Ding, L. Su, A.R. Joshi, A. Singh, B. Reeja-Jayan, J. Beuth,

Parametric analysis to quantify process input influence on the printed densities of binder jetted alumina ceramics, Addit. Manuf. 30 (2019). doi:10.1016/j.addma.2019.100864.

[17] A. Aramian, S.M.J. Razavi, Z. Sadeghian, F. Berto, A review of additive manufacturing of cermets, Addit. Manuf. 33 (2020). doi:10.1016/j.addma.2020.101130.

[18] V.K. Balla, S. Bose, A. Bandyopadhyay, Microstructure and wear properties of laser deposited WC-12%Co composites, Mater. Sci. Eng. A. 527 (2010) 6677–6682. doi:10.1016/j.msea.2010.07.006.

[19] W.J. Lee, E.A. Kim, Y.J. Woo, I. Park, J.H. Yu, T. Ha, Y.S. Choi, H.S. Lee, Effect of different WC particle shapes on laser-exposed microstructures during the directed energy deposition, Powder Metall. 65 (2022) 22–30. doi:10.1080/00325899.2021.1943920.

[20] I. Konyashin, H. Hinners, B. Ries, A. Kirchner, B. Klöden, B. Kieback, R.W.N. Nilen, D. Sidorenko, Additive manufacturing of WC-13%Co by selective electron beam melting: Achievements and challenges, Int. J. Refract. Met. Hard Mater. 84 (2019). doi:10.1016/j.ijrmhm.2019.105028.

[21] E. Uhlmann, A. Bergmann, W. Gridin, Investigation on Additive Manufacturing of Tungsten Carbide.pdf, (n.d.).

[22] R.S. Khmyrov, V.A. Safronov, A. V. Gusarov, Synthesis of Nanostructured WC-Co Hardmetal by Selective Laser Melting, Procedia IUTAM. 23 (2017) 114–119. doi:10.1016/j.piutam.2017.06.011.

[23] S.L. Campanelli, N. Contuzzi, P. Posa, A. Angelastro, Printability and microstructure of selective laser melting of WC/Co/Cr powder, Materials (Basel). 12 (2019). doi:10.3390/ma12152397.

[24] S. Kumar, Process chain development for additive manufacturing of cemented carbide, J.

Manuf. Process. 34 (2018) 121–130. doi:10.1016/j.jmapro.2018.05.036.

[25] N. Ku, J.J. Pittari, S. Kilczewski, A. Kudzal, Additive Manufacturing of Cemented Tungsten Carbide with a Cobalt-Free Alloy Binder by Selective Laser Melting for High-Hardness Applications, Jom. 71 (2019) 1535–1542. doi:10.1007/s11837-019-03366-2.

[26] N. Kang, W. Ma, L. Heraud, M. El Mansori, F. Li, M. Liu, H. Liao, Selective laser melting of tungsten carbide reinforced maraging steel composite, Addit. Manuf. 22 (2018) 104–110. doi:10.1016/j.addma.2018.04.031.

[27] A.J. Cavaleiro, C.M. Fernandes, A.R. Farinha, C. V. Gestel, J. Jhabvala, E. Boillat, A.M.R. Senos, M.T. Vieira, The role of nanocrystalline binder metallic coating into WC after additive manufacturing, Appl. Surf. Sci. 427 (2018) 131–138. doi:10.1016/j.apsusc.2017.08.039.

[28] D. Gu, Q. Jia, Novel crystal growth of in situ WC in selective laser-melted W - C - Ni ternary system, J. Am. Ceram. Soc. 97 (2014) 684–687. doi:10.1111/jace.12828.

[29] C.W. Li, K.C. Chang, A.C. Yeh, J.W. Yeh, S.J. Lin, Microstructure characterization of cemented carbide fabricated by selective laser melting process, Int. J. Refract. Met. Hard Mater. 75 (2018) 225–233. doi:10.1016/j.ijrmhm.2018.05.001.

[30] E. Mendoza Jimenez, B. Reeja-Jayan, J. Beuth, Process development for the laser powder bed fusion of WC-Ni Cermets using sintered-agglomerated powder, Int. J. Appl. Ceram. Technol. (2021) 1–13. doi:10.1111/ijac.13988.

[31] Y. Wang, Y.F. Zhao, Investigation of Sintering Shrinkage in Binder Jetting Additive Manufacturing Process, Procedia Manuf. 10 (2017) 779–790. doi:10.1016/j.promfg.2017.07.077.

[32] T. Do, P. Kwon, C.S. Shin, Process development toward full-density stainless steel parts

with binder jetting printing, Int. J. Mach. Tools Manuf. 121 (2017) 50–60. doi:10.1016/j.ijmachtools.2017.04.006.

[33] C.L. Cramer, H. Armstrong, A. Flores-Betancourt, L. Han, A.M. Elliott, E. Lara-Curzio, T. Saito, K. Nawaz, Processing and properties of SiC composites made via binder jet 3D printing and infiltration and pyrolysis of preceramic polymer, Int. J. Ceram. Eng. Sci. 2 (2020) 320–331. doi:10.1002/ces2.10070.

[34] A. Kumar, Y. Bai, A. Eklund, C.B. Williams, Effects of Hot Isostatic Pressing on Copper Parts Fabricated via Binder Jetting, Procedia Manuf. 10 (2017) 935–944. doi:10.1016/j.promfg.2017.07.084.

[35] A. Yegyan Kumar, Y. Bai, A. Eklund, C.B. Williams, The effects of Hot Isostatic Pressing on parts fabricated by binder jetting additive manufacturing, Addit. Manuf. 24 (2018) 115–124. doi:10.1016/j.addma.2018.09.021.

[36] M. Ziaee, N.B. Crane, Binder jetting: A review of process, materials, and methods, Addit. Manuf. 28 (2019) 781–801. doi:10.1016/j.addma.2019.05.031.

[37] C.L. Cramer, P. Nandwana, R.A. Lowden, A.M. Elliott, Infiltration studies of additive manufacture of WC with Co using binder jetting and pressureless melt method, Addit. Manuf. 28 (2019) 333–343. doi:10.1016/j.addma.2019.04.009.

[38] C.L. Cramer, N.R. Wieber, T.G. Aguirre, R.A. Lowden, A.M. Elliott, Shape retention and infiltration height in complex WC-Co parts made via binder jet of WC with subsequent Co melt infiltration, Addit. Manuf. 29 (2019) 1–6. doi:10.1016/j.addma.2019.100828.

[39] C.L. Cramer, T.G. Aguirre, N.R. Wieber, R.A. Lowden, A.A. Trofimov, H. Wang, J. Yan, M.P. Paranthaman, A.M. Elliott, Binder jet printed WC infiltrated with pre-made melt of WC and Co, Int. J. Refract. Met. Hard Mater. 87 (2020).

doi:10.1016/j.ijrmhm.2019.105137.

[40] R.K. Enneti, K.C. Prough, T.A. Wolfe, A. Klein, N. Studley, J.L. Trasorras, Sintering of WC-12%Co processed by binder jet 3D printing (BJ3DP) technology, Int. J. Refract. Met. Hard Mater. 71 (2018) 28–35. doi:10.1016/j.ijrmhm.2017.10.023.

[41] R.K. Enneti, K.C. Prough, Wear properties of sintered WC-12%Co processed via Binder Jet 3D Printing (BJ3DP), Int. J. Refract. Met. Hard Mater. 78 (2019) 228–232. doi:10.1016/j.ijrmhm.2018.10.003.

[42] R.K. Enneti, K.C. Prough, Wear properties of sintered WC-12%Co processed via Binder Jet 3D Printing (BJ3DP), Int. J. Refract. Met. Hard Mater. 78 (2019) 228–232. doi:10.1016/j.ijrmhm.2018.10.003.

[43] A. Mostafaei, P.R. De Vecchis, K.A. Kimes, D. Elhassid, M. Chmielus, Effect of binder saturation and drying time on microstructure and resulting properties of sinter-HIP binder-jet 3D-printed WC-Co composites, Addit. Manuf. 46 (2021). doi:10.1016/j.addma.2021.102128.

[44] M. Mariani, I. Goncharov, D. Mariani, G. Pietro De Gaudenzi, A. Popovich, N. Lecis, M. Vedani, Mechanical and microstructural characterization of WC-Co consolidated by binder jetting additive manufacturing, Int. J. Refract. Met. Hard Mater. 100 (2021) 105639. doi:10.1016/j.ijrmhm.2021.105639.

[45] A. Kantzas, B. Jonathan, S. Taheeri, Fundamentals of Fluid Flow in Porous Media, 2003.

[46] American Society for Testing and Materials, ASTM C20 - 00(2010) “Standard Test Methods for Apparent Porosity, Water Absorption, Apparent Specific Gravity, and Bulk Density of Burned Refractory Brick and Shapes by Boiling Water,” Refract. Stand. i (2010) 1–3. doi:10.1520/C0020-00R15.2.

[47] ASTM, Standard Guide for Metallographic Sample Preparation of Cemented Tungsten, ASTM Stand. 08 (2012) 24–25. doi:10.1520/B0665-08.2.

[48] ASTM E18/18M-11, Standard Test Methods for Rockwell Hardness of Metallic Materials, ASTM Int. (2018). doi:10.1520/E0018-17E01.

[49] C. Hall, A. Hamilton, Porosity–density relations in stone and brick materials, Mater. Struct. Constr. 48 (2015) 1265–1271. doi:10.1617/s11527-013-0231-1.

[50] C.M. Fernandes, A.M.R. Senos, Cemented carbide phase diagrams: A review, Int. J. Refract. Met. Hard Mater. 29 (2011) 405–418. doi:10.1016/j.ijrmhm.2011.02.004.

[51] X. Lyu, X. Lyu, X. Jiang, X. Jiang, H. Sun, H. Sun, Z. Shao, Z. Shao, Microstructure and mechanical properties of WC-Ni multiphase ceramic materials with NiCl2·6H2O as a binder, Nanotechnol. Rev. 9 (2020) 543–557. doi:10.1515/ntrev-2020-0044.

[52] B. Wittmann, W.D. Schubert, B. Lux, WC grain growth and grain growth inhibition in nickel and iron binder hardmetals, Int. J. Refract. Met. Hard Mater. 20 (2002) 51–60. doi:10.1016/S0263-4368(01)00070-1.

[53] S. Performance, J. Heelan, S.M. Langan, C. Walde, A. Nardi, M. Siopis, R. Barth, T. Landry, A. Birt, Effect of WC-Ni Powder Composition and Preparation, (2020).

[54] V.B. Voitovich, V. V. Sverdel, R.F. Voitovich, E.I. Golovko, Oxidation of WC-Co, WC-Ni and WC-Co-Ni Hard Metals in the Temperature Range 500-800°C, Int. J. Refract. Met. Hard Mater. 14 (1996) 289–295. doi:10.1016/0263-4368(96)00009-1.